Temporal I_{max}-Derived FOD Radiomics for Classification of Breast Cancer Treatment Response: A 4D DCE-MRI Study

B. Priyadharshini[1], A. Mythili[1] and K. R. Anandh[2]

1. School of Electronics Engineering, Vellore Institute of Technology, Vellore, Tamil Nadu, India
2. Department of Radiology, Cincinnati Children's Hospital Medical Centre, Cincinnati, Ohio, USA
mythili.asaithambi@vit.ac.in, priyadharshini.b2020a@vitstudent.ac.in, anandhmurali@gmail.com

***Abstract*— Breast cancer is the most prevalent genetic malignancy, causing cancer-related fatalities among women worldwide. This highlights the importance of early detection and accurate response evaluation in improving patient prognosis and long-term survival rates. Dynamic Contrast-Enhanced Magnetic Resonance Imaging (DCE-MRI) captures voxel-wise temporal insights that reveal perfusion heterogeneity and vascular permeability, thereby facilitating the discrimination of pCR (pathological complete response) and non-pCR (non-pathological complete response) when evaluating treatment response. Accordingly, this work proposes a temporally derived fractional order derivative (FOD) based radiomics model for breast cancer treatment response classification. Herein, the model is primarily validated using the QIN Breast DCE-MRI dataset, consisting of a limited patients (pCR=3, non-pCR=7) scanned at 32 time points. However, each patient encompasses prominent temporal insights, assisting in validating the model. Initially, the I_{max} maps are extracted from 4D DCE-MRIs, which are utilized for computing the Fractional Order Derivative (FOD) gradient images. A comprehensive set of radiomic features was extracted from the FOD gradient images corresponding to two chemotherapy cycles (Visit 1 and Visit 2).**

Generally, the FOD images provide complementary information, enhancing the predictive ability of the radiomics model. Further, a robust feature dimensionality reduction technique is incorporated for selecting optimal features from the combined feature sets (Visit 1, Visit 2, and Δ(V2, V1). The selected optimal features are utilized for training and testing the classification models, namely, Support Vector Machine (SVM) kernels (Linear, RBF, polynomial), Logistic Regression, and Random Forest for classifying pCR and non-pCR classes. Further, the classifying models are evaluated by metrics, obtaining an interpretable and balanced model. Hence, the clinical application of the proposed model aids personalised therapy and improves the survival rate.

Keywords*— *breast cancer, FOD, Imax map, non-pCR, pCR, radiomics, feature selection, classification.

I. Introduction

By the year 2020 to 2040, the World Health Organization (WHO) intends to avert 2.5 million breast cancer fatalities, overall reducing 2.5% each year. Early detection and treatment planning aid in breast conservation surgery and increase the survival rate of cancer patients [1]. The breast cancer patients are categorized as pCR and non-pCR, referring to the absence and existence of residual invasive cancer after neo-adjuvant therapy, respectively [2].

DCE-MRI, a non-invasive technique, scans voxel-wise subtle temporal changes from the breast region and acts as a versatile biomarker facilitating perfusion-induced therapies while evaluating treatment response in breast cancer patients. There are several temporal parameters (e.g., I_{max}, Time To Peak) that quantify the tumor's necrotic and hypoxic regions and are often correlated with proliferation factor and survival outcome [3][4]. Particularly, the maximum intensity parameter often resembles the peak vascular enhancements in highly aggressive tumors [5].

In addition, the advent of FODs [6] in medical image analysis has become an effective tool for capturing multiscale structural patterns compared to integer order derivatives. It eases the higher-order textural patterns, considering global and local variations, thereby demonstrating the intricate tumor biology that is deemed essential for treatment assessment in breast cancer patients [7][8].

Radiomics quantifies spatial and textural insights from medical images, while FOD-based gradients capture local intensity transitions. Their combination synergistically enhances feature sensitivity to microstructural and perfusion-related heterogeneity, thereby improving the predictive power of the imaging biomarker in assessing treatment response. For instance, the most recent research has formulated the GL fractional differential gradient operator, generating a pixel-sized mask for correlating neighboring pixels [9]. However, FODs to enhance the medical images introduce a novel application and necessitate further research.

With the emergence of Machine Learning approaches, leveraging the primary spatiotemporal features as rich biomarkers, assessing the pathological complete response has become feasible [10]. The author from [11] had extracted 348 radiomics features from the tumor and peritumor regions that quantify the temporal textural patterns and heterogeneity. Lately, the logistics regression was trained and tested for treatment assessment and molecular subtype classification. An integrated kinetic and quantum-Raina's polynomial (QRP) feature [12] is implemented in DCE-MRI breast

cancer classification, achieving an accuracy of 97.4 % over 300 patients. Nevertheless, the above research involves the feature extraction from the original images, whereas this work proposes extracting from a transformed image. Similarly, the deep networks play a key role in assessing pCR and non-pCR categories by combining clinical and pathological data [13]. For instance, ResNet18 [14] combined transfer learning to assess the NAC response, with the performance of 87 % using an SVM classifier. A multi-modal fusion for pre-treatment and early treatment, achieving 92 % AUC. The author performed a comparison of multimodal with unimodal DL [13].

The proposed framework incorporates an analytical segmentation model and a learning-based feature extraction, selection, and classification model for classifying patients with pCR and those with non-pCR. The rationale for the energy-based analytical model is due to its transparency, interpretability, and flexibility in delineating tumor boundaries more precisely, which are deemed essential for medical image processing. Contrastingly, the choice of machine learning (ML) methods for feature extraction, selection, and classification is owing to the intricate structural complexity posed by the tumors. Generally, ML models are excellent at learning complex and non-linear patterns extracted from radiomics features, which are multi-dimensional and impact the feature space extracted from the segmented region to assess the treatment response in breast cancer patients. This combinatorial arrangement of analytical and data-driven approaches in the proposed discriminative model leverages the effectiveness of both paradigms, which are crucial for real-time applications in decision-making.

II. Materials and Methods

The proposed workflow for PCR and non-PCR classification is chronologically described in this section.

A. Dataset and Imaging Protocols

The dataset utilized for this analysis is adopted from The Cancer Image Archive (TCIA) repository [15], which is publicly available for researchers. The QIN Breast DCE-MRI dataset consists of 10 patients, each scanned at 32 time points for two Visits (V1 and V2), forming a 4D DCE-MRI. The major utilization of this dataset is to evaluate breast cancer therapy after neo-adjuvant chemotherapy. Accordingly, Table 1 presents the imaging protocol associated with the QIN Breast DCE-MRI dataset.

Table 1. Dataset and image acquisition parameters

Parameter Name	Parameter Values
Image Strength (Patients)	10
Scanner	Siemens 3T
Sequence	TWIST
TR (ms)	2.9
TE (ms)	6.2
Flip Angle (degree)	10
FOV (mm)	300–340
Slice Thickness (mm)	1.4
Image Dimensions	320 × 320
Slice Number	112–120

B. I_{max} map Calculation

Generally, I_{max} maps are computed as the maximum signal intensity observed across all temporal frames of the DCE-MRI sequence, providing a robust kinetic descriptor of peak enhancement behavior. Such I_{max} maps are calculated by $I_{max}(x,y,z) = \max_t I(x,y,z,t)$ statistical formula where t =1,2,3,4..., N, representing a maximum intensity at each voxel.

C. Fractional order derivative (FOD) gradient image

The calculated I_{max} maps were processed using First-Order Derivative (FOD) gradient transformations in the X, Y, and Z. Accordingly, this work utilizes the Grünwald–Letnikov (GL) fractional derivative that is appropriate for a 3D image with each mask of size 3x3x3. The FOD of order α in all three directions is calculated by using the formula as shown in Eqn. (1 to 3).

$$D_x^{\alpha} f(x,y,z) = \sum_{k=0}^{n} (-1)^k \left(\frac{\alpha}{k}\right) f(x-k,y,z) \quad (1)$$

$$D_y^{\alpha} f(x,y,z) = \sum_{k=0}^{n} (-1)^k \left(\frac{\alpha}{k}\right) f(x,y-k,z) \quad (2)$$

$$D_z^{\alpha} f(x,y,z) = \sum_{k=0}^{n} (-1)^k \left(\frac{\alpha}{k}\right) f(x,y,z-k) \quad (3)$$

Herein, $\left(\frac{\alpha}{k}\right) = \frac{\Gamma(\alpha+1)}{\Gamma(k+1)\Gamma(\alpha-k+1)}$, where $\Gamma(.)$, is a Gamma function that generalizes the factorial binomial coefficient. This coefficient extends the concept of integer-order differentiation to fractional-order differentiation, allowing smooth transitions between derivative orders. The resulting weights $w_k = (-1)^k \left(\frac{\alpha}{k}\right)$ define the fractional derivative mask, where 'α' controls the differentiation order and 'k' indexes the discrete neighborhood contribution.

D. Mask Generation

The tumor region from the breast DCE-MRI is extracted by an analytical segmentation model, named as Bezier-tuned Energy Functionals optimized via variational minimax for Volumetric Breast Tumor Segmentation

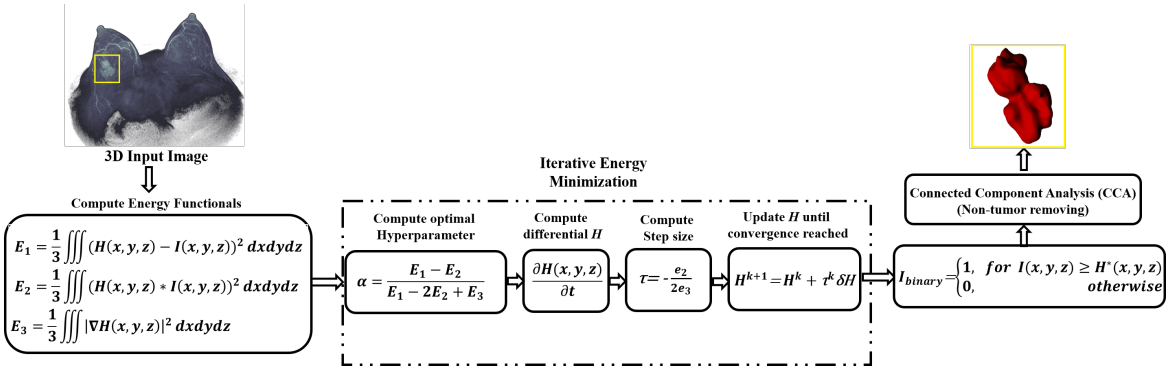

Figure 1. BEFVBTS model for tumor segmentation and mask generation.

(BEFVBTS) [16][17]. The model proposes a convex and non-linear energy functional engaging data fidelity and L2 norm regularization terms. Accordingly, the model's cost function is shown in Eq. (4). The BEFVBTS model's flow diagram is depicted in Fig. 1.

$$E(H;\alpha) = (1-\alpha)^2 E_1 + 2\alpha(1-\alpha)E_2 + \alpha^2 E_3 \qquad (4)$$

where, $I(x,y,x)$ is the input image, $H(x,y,x)$ is the Hessian of the image, 'α' here is the weight parameter, 'τ' is the step size, and $E_1, E_2, and\ E_3$ are the energy functionals. The proposed cost function shown in Eq. (4) is minimized iteratively until convergence is reached, thereby obtaining the optimal 'α' and heterogeneous volume, H. The post-processing steps, such as binarization and Connected Component Analysis (CCA), are incorporated in the model for precise extraction of the tumor from surrounding non-tumor regions.

E. Feature Extraction

Further, the generated binary masks are superimposed on the FOD-transformed image to extract the FOD-transformed tumor regions. From the resulting ROI, a total of 572 radiomics features from 2 different classes (FOD and Log filtered image) were extracted for 2 cycles of chemotherapy. Herein, Pyradiomics, an open source [18], is engaged in extracting first-order, shape, and texture features from the transformed tumor region.

F. Feature Selection

The extracted radiomics features are huge, hence, the LASSO (Least Absolute Shrinkage and Selection Operator) model is utilized to select the most significant features [19]. LASSO aims to minimize the residual sum of squares by imposing an L1 penalty term, as shown in Eq. (5), which promotes sparse feature selection and reduces model overfitting.

$$\max_{\alpha}\left\{\frac{1}{2n}\sum_{i=1}^{n}\left(y_i - \alpha_0 - \sum_{j=1}^{p} x_{ij}\alpha_j\right)^2 + \lambda\sum_{j=1}^{p}|a_j|\right\} \qquad (5)$$

In Eq. (5), α is the weight parameter and λ is the regularization parameter. A total of 1716 radiomics features combining Visit 1, Visit 2 cycles, and **Δ** (Visit 2 - Visit 1) (572x3 = 1716) were extracted and utilized for training the classification model.

G. Classification Models

The robust classification models, SVM and its variants, Logistic Regression, and Random Forest, are trained and tested by the selected optimal features. Due to the limited patient strength, Leave-One-Out Cross-Validation (LOOCV) is employed to ensure robust and unbiased performance estimation [20].

H. Performance Metrics

The metrics, such as Accuracy, F1-score, Precision, and Recall, were computed to comprehensively assess the classification performance of the models, as shown in Eqs. (6 - 9):

$$Accuracy = \frac{TP + TN}{TP + TN + FP + FN} \qquad (6)$$

$$F1 - score = \frac{2TP}{2TP + FP + FN} \qquad (7)$$

$$Precision = \frac{TP}{TP + FP} \qquad (8)$$

$$Recall = \frac{TP}{TP + FN} \qquad (9)$$

where, TP is "True Positive," TN is "True Negative," FP is "False Positive," and FN is "False Negative."

III. Results and Discussion

A. Tumor Characterization using I_{max} and FOD

The I_{max} maps are calculated from a 4D DCE-MRI image, indicating tumor perfusion and vascularization in contrast dynamics. Additionally, to enhance edge information, the fractional order derivative of order α=0.5 is applied to I_{max} maps, capturing microstructural patterns. Fig. 2 depicts the visuals from I_{max} and FOD-derived gradient images. The tumor in the I_{max} map

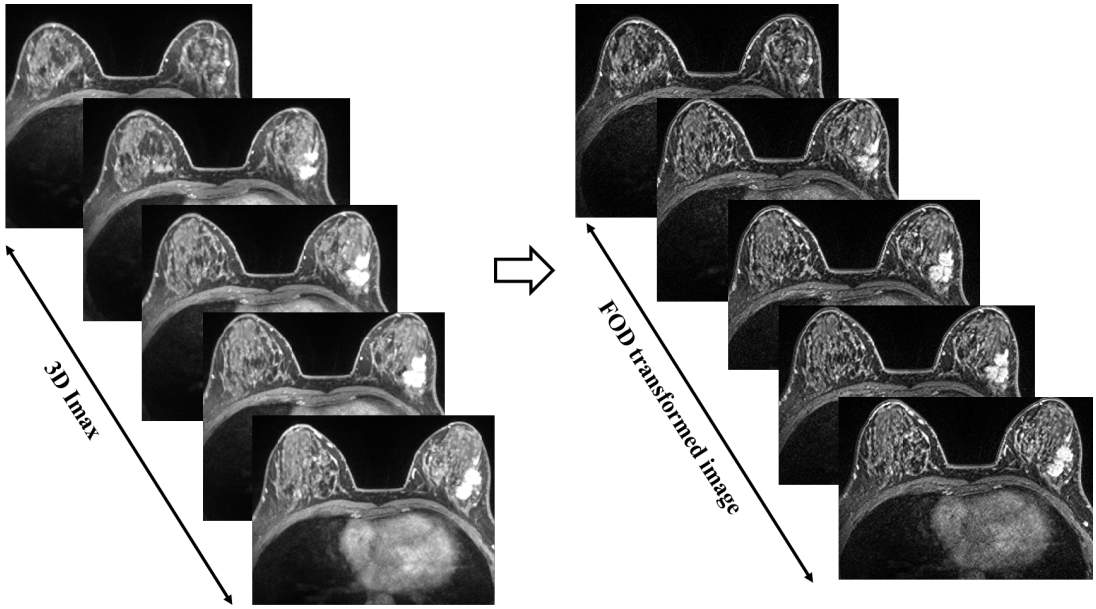

Figure 2. Visualization of 3D I_{max} and FOD-derived gradient maps from DCE-MRI.

shows a strong enhancement corresponding to high vascular activity, while the FOD map emphasizes intensity gradients that delineate tumor margins and internal heterogeneity.

B. Feature Extraction Summary

Radiomics features are extracted from 2 classes, namely, the FOD transformed image and the multi-scale LoG version of FOD. Table 2 depicts the summary of radiomics features extracted across various classes, the name of the group, and the total count in each class. The scale ranges from 1-5mm and bin width=22, captures the enhanced textural patterns highlighting the intricate tumor heterogeneity at different spatial frequencies.

Table 2. Summary of extracted radiomic features

Feature Class	Feature Split-up	Total Features
Original image class	First order: 18 Shape: 14 GLCM: 24, GLDM: 14 GLRLM: 16, GLSZM: 16 NGTDM: 5	107
Log filtered image (1–5 mm)	First order: 18 GLCM: 24, GLDM: 14 GLRLM: 16, GLSZM: 16 NGTDM: 5 (for each mm scale)	93 × 5 = 465

C. Analysis of the LASSO Model.

The plot in Fig. 3(a) depicts the feature shrinkage process as alpha increases, projecting the sparsity of the model.

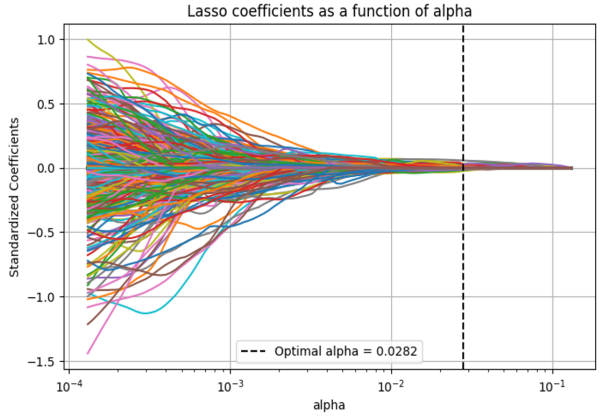

(a)

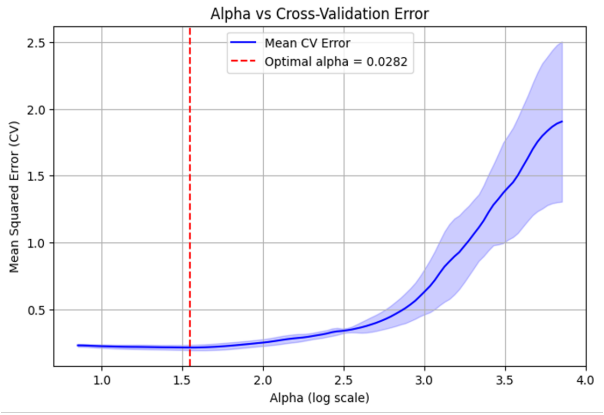

(b)

Figure 3. Visualization of LASSO regularization showing (a) Coefficient variation with α and (b) Cross-validation error for finding optimal α value.

The features leading to zero indicate the amount of contribution in the classification process. The plot in Fig. 3(b) depicts the relationship between alpha and the mean square error during cross-validation. After model tuning, the best alpha (0.0282) chosen by the model ensures the balance between generalization and model complexity. The shaded blue region in Fig. 3(b) represents the variation in the error, and the dark blue line indicates the mean cross-validation (CV) error. The model selected 9 optimal features from 1716 combined features that are listed in Table 3, in the format, feature name → class→ feature type. The abbreviations for the terms used in Table 3 are GLNN-Gray Level Non-Uniformity Normalized, GLV-Gray Level Variance, LDE-Large Dependence Emphasis, SAE-Small Area Emphasis, RLNN-Run Length Non-Uniformity Normalized, and SRLGE- Short Run Low Gray Level Emphasis. The selected radiomics feature values are significant in classifying pCR and non-pCR breast cancer patients.

D. Classification Results

Following a robust and reliable feature selection process, various classifiers, SVM, Logistic regression, and Random Forest, are trained and tested for classifying pCR and non-pCRs. Tables 4 and 5 present the optimized hyperparameters and performance metrics details of the classification models. The SVM kernels were adjusted for the regularization parameter C and kernel-specific parameters (γ and degree), while Logistic Regression and Random Forest were tuned for convergence stability and depth control, respectively. Each kernel performs uniquely, linear possesses simple separability, and acts as a baseline, while the polynomial exhibits a moderate feature relationship. The other variant, RBF, mainly captures the intricate and non-linear feature relationship among the extracted textural information, thereby facilitating an unbiased performance analysis in the classification process. The above claim is depicted in Table 5, where all classifiers demonstrated strong discriminative performance under Leave-One-Out Cross-Validation (LOOCV). Furthermore, the permutation-based significance analysis (*p_perm* less than 0.05) validates that the observed classification performance is statistically meaningful and not due to random chance, as shown in Fig. 4 (b). Similarly, Table 4 summarizes the key configurations and performance insights of various classification models used in the evaluation, along with class balance handling and optimization settings.

Table 3. Feature class and category distribution of LASSO-selected features.

Feature Name	Class → Type
V1_GLNN.9	log-sigma-4-0-mm-3D → GLSZM
V1_GLV.14	log-sigma-4-0-mm-3D → GLSZM
V2_SAE.5	log-sigma-5-0-mm-3D → GLSZM
Δ_Minimum	FOD loaded image → first-order
Δ_DependenceVariance.1	log-sigma-1-0-mm-3D → GLDM
Δ_LDE.1	log-sigma-1-0-mm-3D → GLDM
Δ_RLNN.1	log-sigma-1-0-mm-3D → GLRLM
Δ_SRLGE.1	log-sigma-1-0-mm-3D → GLRLM
Δ_ZonePercentage.5	log-sigma-5-0-mm-3D → GLRLM

The statistical test shows a p-value of 0.0370, which is statistically significant. Similarly, there is a necessity to check feature importance in the classification model, demonstrating the high significance of difference features from visit 1 and visit 2, as shown in Fig. 5. However, the high feature importance of the models relies on the Short Run Low Gray Level Emphasis feature from the log sigma class and GLRLM type. The ROC curves shown in Fig. 4 (a) demonstrate near-perfect classification performance, with AUC values approaching 1.0 across all classification models. While such high AUC scores indicate strong separability between pCR and non-pCR feature distributions, they may also suggest potential model overfitting, particularly given the limited dataset size.

In summary, the proposed FOD-based radiomics model improves clinical interpretability by establishing a stronger association between the extracted radiomic features and the physiological parameters of DCE-MRI, particularly the I_{max} parameter, which reflects tumor vascular and perfusion dynamics.

IV. Summary

This study demonstrates the effective classification of patients with pCR and non-pCR using temporal maps and their corresponding fractional-order derivative (FOD) representations. The incorporation of FODs enhances subtle textural and kinetic contrasts within DCE-MRI, capturing underlying physiological heterogeneity that conventional intensity maps may overlook. Radiomic features extracted from these transformed images served as informative and biologically relevant biomarkers, enabling the development of a robust physiologically interpretable classification model. Future work will validate the model on larger multi-institutional cohorts, apply harmonization to reduce scanner variability, and improve generalizability through multi-parametric integration to enable clinical translation and personalized treatment planning.

Table 4. Summary of tuned hyperparameters, support vectors, and model characteristics.

Model	Key Hyperparameters	Support Vectors	Additional Insights
Linear SVM	C = 1.0, kernel = linear	5	Support vectors per class: [3, 2]
RBF SVM	C = 10, γ = 0.1	9	Support vectors per class: [6, 3]
Polynomial SVM	C = 1.0, degree = 3, γ = scale	6	Support vectors per class: [4, 2]
Logistic Regression	C = 1.0, penalty = L2	–	max_iter = 1000
Random Forest	n_estimators = 200, max_depth = 10	–	class_weight = balanced

Table 5. Comparative performance summary of classification models (LOOCV, n=10)

Model	Accuracy (%)	Precision (%)	Recall (%)	F1-score (%)	p_{perm}
Linear SVM	98.4 ± 1.8 (94.1–100.0)	97.2 ± 2.6 (93.0–100.0)	96.8 ± 2.9 (91.5–100.0)	97.3 ± 2.5 (92.4–100.0)	0.048
Polynomial SVM	97.5 ± 2.4 (91.3–100.0)	96.7 ± 2.8 (91.0–100.0)	97.1 ± 2.5 (92.0–100.0)	96.9 ± 2.7 (91.2–100.0)	0.013
RBF SVM	99.2 ± 1.1 (97.2–100.0)	98.5 ± 1.6 (95.1–100.0)	99.1 ± 0.9 (97.5–100.0)	98.6 ± 1.4 (95.3–100.0)	0.020
Logistic Regression	99.3 ± 1.0 (97.0–100.0)	99.0 ± 1.2 (96.5–100.0)	99.1 ± 0.8 (97.3–100.0)	98.8 ± 1.5 (95.4–100.0)	0.029
Random Forest	99.4 ± 0.9 (97.4–100.0)	99.2 ± 1.0 (97.0–100.0)	99.3 ± 1.1 (97.2–100.0)	99.1 ± 1.0 (97.0–100.0)	0.011

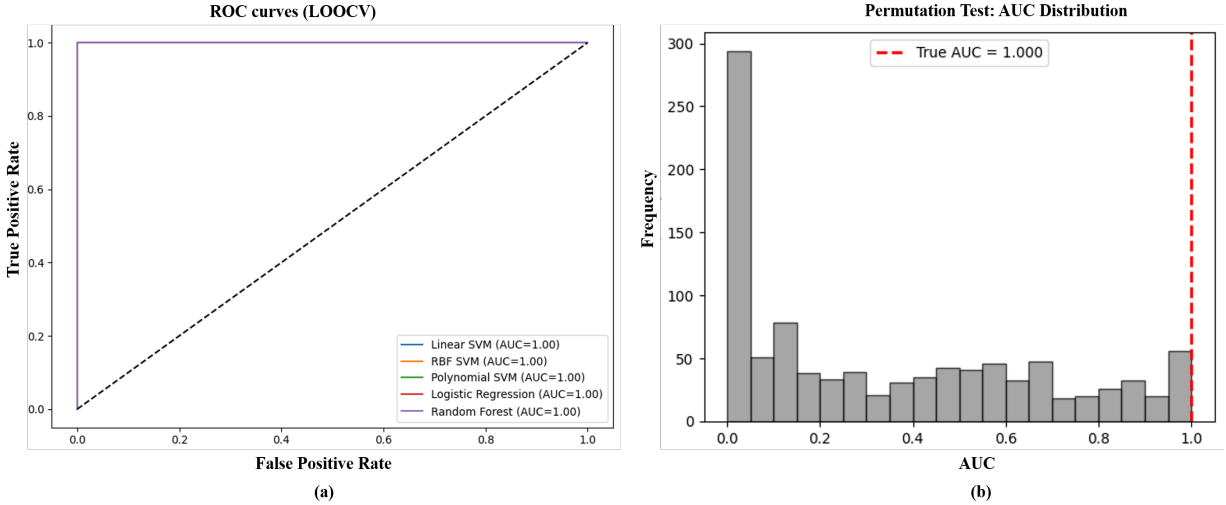

Figure 4. (a) Comparison of ROC curves for multiple classifiers. (b) Model robustness check using a permutation test.

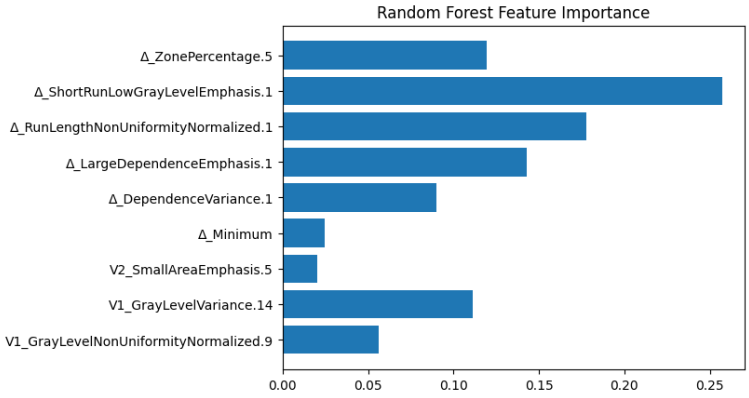

Figure 5. Feature importance of LASSO-selected features.

REFERENCES

[1] R. L. Siegel, A. N. Giaquinto, and A. Jemal, "Cancer statistics, 2024," *CA. Cancer J. Clin.*, vol. 74, no. 1, pp. 12–49, 2024, doi: 10.3322/caac.21820.

[2] M. Caballo, W. B. G. Sanderink, L. Han, Y. Gao, A. Athanasiou, and R. M. Mann, "Four-Dimensional Machine Learning Radiomics for the Pretreatment Assessment of Breast Cancer Pathologic Complete Response to Neoadjuvant Chemotherapy in Dynamic Contrast-Enhanced MRI.," *J. Magn. Reson. Imaging*, vol. 57, no. 1, pp. 97–110, Jan. 2023, doi: 10.1002/jmri.28273.

[3] J. P. B. O'Connor *et al.*, "DCE-MRI biomarkers of tumour heterogeneity predict CRC liver metastasis shrinkage following bevacizumab and FOLFOX-6.," *Br. J. Cancer*, vol. 105, no. 1, pp. 139–145, Jun. 2011, doi: 10.1038/bjc.2011.191.

[4] F. Khalifa *et al.*, "Models and methods for analyzing DCE-MRI: a review.," *Med. Phys.*, vol. 41, no. 12, p. 124301, Dec. 2014, doi: 10.1118/1.4898202.

[5] X. Li *et al.*, "Analyzing Spatial Heterogeneity in DCE- and DW-MRI Parametric Maps to Optimize Prediction of Pathologic Response to Neoadjuvant Chemotherapy in Breast Cancer.," *Transl. Oncol.*, vol. 7, no. 1, pp. 14–22, Feb. 2014, doi: 10.1593/tlo.13748.

[6] J. Guan, J. Ou, Z. Lai, and Y. Lai, "Medical Image Enhancement Method Based on the Fractional Order Derivative and the Directional Derivative," *Int. J. Pattern Recognit. Artif. Intell.*, vol. 32, no. 03, p. 1857001, 2018, doi: 10.1142/S021800141857001X.

[7] D. Tian, "Medical Image Segmentation Based on Fractional-Order Derivative," no. Ap3er, pp. 453–456, 2015.

[8] T. Bento and D. Val, "Fractional order image processing of medical images," pp. 6–12.

[9] A. Singh, M. Sajid, N. K. Tiwari, and A. Shukla, "Single channel medical images enhancement using fractional derivatives.," *PLoS One*, vol. 20, no. 5, p. e0319990, 2025, doi: 10.1371/journal.pone.0319990.

[10] S. Feuerriegel *et al.*, "Causal machine learning for predicting treatment outcomes.," *Nat. Med.*, vol. 30, no. 4, pp. 958–968, Apr. 2024, doi: 10.1038/s41591-024-02902-1.

[11] J. Park *et al.*, "Machine Learning Predicts Pathologic Complete Response to Neoadjuvant Chemotherapy for ER+HER2- Breast Cancer: Integrating Tumoral and Peritumoral MRI Radiomic Features.," *Diagnostics (Basel, Switzerland)*, vol. 13, no. 19, Sep. 2023, doi: 10.3390/diagnostics13193031.

[12] A. M. Hasan, N. K. N. Al-Waely, H. K. Ajobouri, R. W. Ibrahim, H. A. Jalab, and F. Meziane, "A classification model of breast masses in DCE-MRI using kinetic curves features with quantum-Raina's polynomial based fusion," *Biomed. Signal Process. Control*, vol. 84, p. 105002, 2023, doi: https://doi.org/10.1016/j.bspc.2023.105002.

[13] E. Krasniqi *et al.*, "Multimodal deep learning for predicting neoadjuvant treatment outcomes in breast cancer: a systematic review.," *Biol. Direct*, vol. 20, no. 1, p. 72, Jun. 2025, doi: 10.1186/s13062-025-00661-8.

[14] M. Lv *et al.*, "Deep learning model for the early prediction of pathologic response following neoadjuvant chemotherapy in breast cancer patients using dynamic contrast-enhanced MRI.," *Front. Oncol.*, vol. 15, p. 1491843, 2025, doi: 10.3389/fonc.2025.1491843.

[15] K. Clark *et al.*, "The cancer imaging archive (TCIA): Maintaining and operating a public information repository," *J. Digit. Imaging*, vol. 26, no. 6, pp. 1045–1057, Dec. 2013, doi: 10.1007/s10278-013-9622-7.

[16] P. Babu, M. Asaithambi, and S. Mogappair Suriyakumar, "Automated 3D Tumor Segmentation From Breast DCE-MRI Using Energy-Tuned Minimax Optimization," *IEEE Access*, vol. 12, pp. 87532–87544, 2024, doi: 10.1109/ACCESS.2024.3417488.

[17] P. Babu, M. Asaithambi, and S. Mogappair Suriyakumar, "Contextual Regularization-Based Energy Optimization for Segmenting Breast Tumor in DCE-MRI," *IEEE Access*, vol. 13, pp. 51986–52005, 2025, doi: 10.1109/ACCESS.2025.3553035.

[18] J. J. M. van Griethuysen *et al.*, "Computational Radiomics System to Decode the Radiographic Phenotype.," *Cancer Res.*, vol. 77, no. 21, pp. e104–e107, Nov. 2017, doi: 10.1158/0008-5472.CAN-17-0339.

[19] B. Priyadharshini, A. Mythili, and K. R. Anandh, "Performance Analysis of Low and High-Grade Breast Tumors Using DCE MR Images and LASSO Feature Selection," in *2023 IEEE Signal Processing in Medicine and Biology Symposium (SPMB)*, 2023, pp. 1–6. doi: 10.1109/SPMB59478.2023.10372756.

[20] V. Lumumba, D. Kiprotich, M. Mpaine, N. Makena, and M. Kavita, "Comparative Analysis of Cross-Validation Techniques: LOOCV, K-folds Cross-Validation, and Repeated K-folds Cross-Validation in Machine Learning Models," *Am. J. Theor. Appl. Stat.*, vol. 13, no. 5, pp. 127–137, 2024, doi: 10.11648/j.ajtas.20241305.13.